SolarPACES 2024, 30th International Conference on Concentrating Solar Power, Thermal, and Chemical Energy Systems

Solar Fuels and Chemical Commodities

https://doi.org/10.52825/solarpaces.v3i.2384

Two-Step Thermochemical Conversion of CO_2 Using a Novel $Nd_{1-x}Sr_xMnO_3$ Perovskite

Muhammad Usman[1,2], Giovanni Palmisano[1,2], Georgios Karanikolos[3], Stéphane Abanades[4], and Khalid Al-Ali[1,2,*]

[1]Khalifa University of Science and Technology, Chemical and Petroleum Engineering, Abu Dhabi, UAE

[2]Research and Innovation on CO_2 and H_2 (RICH) Center, Khalifa University, Abu Dhabi, UAE

[3]University of Patras, Chemical Engineering, Patras, Greece

[4]Laboratoire Procédés, Matériaux et Energie Solaire France

*Correspondence: Khalid Al-Ali, khalid.alali@ku.ac.ae

Abstract. A two-step thermochemical splitting process of doped and undoped neodymium-based manganite perovskites was investigated using thermogravimetric analysis. The samples were synthesized using a modified Pechini method and characterized by XRD, SEM and EDS analysis before redox testing. The results showed that 40% Sr-doped $Nd_{0.6}Sr_{0.4}MnO_3$ outperformed the other samples, achieving 103.7 μmol-O_2/g during thermal reduction and 189.2 μmol-CO/g during thermal oxidation, with a re-oxidation yield of 91.2%.

Keywords: Thermochemical Conversion, CO_2 Splitting, Perovskites, Neodymium-Manganite

1. Introduction

The global energy infrastructure is experiencing a significant transformation towards a more renewable and greener sustainable future [1], [2], [3]. Thermochemical energy storage (TCES) systems, when integrated with concentrated solar power (CSP) plants, have the potential to store surplus solar energy for continuous supply of power during nocturnal periods by actively storing the solar energy diurnally [4], [5], [6]. These storage systems offer the advantage of utilizing the full solar spectrum (unlike photovoltaics, which only capture part of it) along with sequestering significant amounts of CO_2 by converting it into solar fuel, such as CO in a cyclic manner so as to minimize the greenhouse gas imprint on the environment [7], [8]. A two-step thermochemical energy storage system works by leveraging the reversibility of a chemical reaction, where energy input—typically from high-temperature solar heat collected by a CSP plant—drives the reaction forward. The products of the reaction are stored separately which can readily be combined to release back the energy during the energy input interlude i.e., nocturnal period when sun is not available. This process is known as the charging and discharging cycle. Among various available TCES systems, the two-step thermochemical conversion of CO_2 via perovskite materials stands out due to its higher reported fuel yields compared to other oxygen-exchange materials, such as ceria and metal oxides.

Generally, perovskites are ABO_3-type materials, where A is a 12-fold coordinated alkali, alkaline earth, or Lanthanide metal cation, and B is a 6-fold coordinated transition metal cation. Partial doping can occur at both the A and B sites, resulting in a $AA'BB'O_3$ structure, where A' and B' represent dopant cations. Therefore, these materials represent a diverse combination of cations with tunable properties, offering immense potential with solutions to current day energy storage challenges. Equation 1 shows the first reaction in a two-step thermochemical CO_2 splitting process, known as thermal reduction. In this step, the perovskite material (ABO_3) is subjected to high temperatures under relatively low oxygen partial pressures. As a result, the perovskite material thermally reduces to oxygen deficient form i.e., $ABO_{3-\delta}$ where δ represents oxygen non-stoichiometry. In the subsequent step, as shown in Equation 2, the reduced perovskite is re-oxidized at relatively lower temperatures in a CO_2 environment.

$$ABO_3 + \Delta H_{reduction} \xrightarrow{low\ p_{O_2}} ABO_{3-\delta} + \frac{\delta}{2} O_2(g) \tag{1}$$

$$ABO_{3-\delta} + \delta(H_2O/CO_2) \xrightarrow{exothermic\ process} ABO_3 + \delta(H_2/CO) \tag{2}$$

However, despite the higher fuel yields, several challenges, such as slow kinetics and material sintering, still require further research attention. This study focuses on investigating a novel perovskite composition, $Nd_{1-x}Sr_xMnO_3$ (where x = 0, 0.2, 0.4, 0.6, 0.8), in a two-step thermochemical redox process for converting CO_2 into CO, using a thermogravimetric analyzer.

2. Experimental section

2.1 Chemicals

Chemicals used for the synthesis of perovskite powders, including Nd_2O_3 (99.9%), $Sr(NO_3)_2$ (99.999%), $Mn(NO_3)_2.4H_2O$ & (98-102%) & ethylene glycol (99%), were purchased from Glentham Chemicals. Citric acid (CA) (99%) was obtained from Sigma-Aldrich.

2.2 Material Synthesis

The perovskite powders were synthesized using a modified Pechini method [9], [10]. Metal salt precursors were mixed with a chelating agent i.e., citric acid (CA) and ethylene glycol (EG) as complexing agent in the following molar ratio: CA:M:EG = 1.5:1:1. Typically, the metal precursors were dissolved in deionized water with a fixed mass ratio of M:H_2O = 1:6.

The mixture was continuously stirred for 10 minutes and heated to 60℃, after which EG was added. The mixture was then heated to 120℃ until a viscous colored sol was obtained. This sol was subjected to polyesterification to form a polymeric resin by heating it at 250℃ for 120 minutes. The resulting resin was crushed into powder using an agate mortar. The powder was air-calcined in a muffle furnace at 1400℃ for 6 hours, with a ramp rate of $5℃/min$. After calcination, the product was again crushed into powder form using an agate mortar and subjected to further characterization and testing. Table 1 outlines the sample formulations.

2.3 Characterization

Various physico-chemical characteristics of the perovskite powder, including its crystalline structure, chemical composition, and morphology, were obtained and compared. The room temperature powder XRD pattern was recorded using a PANalytical Empyrean XRD diffractometer with Cu Kα radiation (wavelength λ = 0.15418 nm), a tube current of 35 mA, and a potential of 45 kV, in the 2θ range of 20° to 80°. The PXRD data were compared with the ICDD-OCD database. A JEOL JSM-7610F scanning electron microscope was used for evaluating the sample morphology, while Energy dispersive X-ray (EDX) spectroscopy was employed to study the composition of the synthesized samples.

2.4 Redox testing

The reactivity of the air-calcined perovskite samples was studied using thermogravimetric analysis (TGA) with a SETARAM SETSYS apparatus. Approximately 100 mg of the sample was placed in a platinum crucible. The samples were subjected to the thermal reduction step in the TGA at 1400℃ with a heating ramp of 20 ℃/min under an inert argon gas flow of 0.020 NL/min, with 99.999% purity and less than 2 ppm O_2. The temperature was kept constant at 1400 ℃ for 45 minutes. Subsequently, in the oxidation step, the temperature was lowered to 1050 ℃ with a ramp of 20 ℃/min, and the gas environment was switched to 50% CO_2 in Ar at a total flow of 0.020 NL/min for 60 minutes, completing the first cycle. During the second cycle, the temperature was raised from 1050 ℃ to 1400 ℃ under argon environment, and thermal reduction was carried out as before for 45 minutes. A similar re-oxidation step was carried out, lowering the temperature from 1400 ℃ to 1050 ℃ under CO_2/Ar environment. During all these redox processes, mass changes in the perovskite samples were recorded. The mass changes during the thermal reduction/oxidation process, caused by the release or uptake of oxygen, were quantified in terms of n_{O_2} and n_{CO}. Here, n_{O_2} represents the amount of oxygen produced per gram of perovskite during thermal reduction step, while n_{CO} represents the amount of CO produced per gram the sample during the thermal oxidation step. Equations (3) and (4) show how n_{O_2} and n_{CO} can be calculated from the thermogravimetric data.

$$n_{O_2} = \frac{\Delta m_{loss\ during\ TR}}{m_{sample} \cdot M_{O_2}} \tag{3}$$

$$n_{CO} = \frac{\Delta m_{gain\ during\ TO}}{m_{sample} \cdot M_{O}} \tag{4}$$

Δm represents the mass loss/gain during thermal reduction/oxidation, m_{sample} is the initial mass of the sample placed in the platinum crucible, M_{O_2} and M_O are the molecular masses of O_2 and O, respectively. Since the kinetics of oxidation step in perovskite samples are reportedly very slow and require extended operation times, the material recovery is quantified using the re-oxidation yield, as shown in Equation 5. This re-oxidation yield measures the extent to which the oxygen released by the perovskite material during thermal reduction is re-absorbed, indicating the relative completion of the oxidation process.

$$re - oxidation\ yield\ (\%) = \frac{1}{2}\left(\frac{n_{CO}}{n_{O_2}}\right) \times 100\% \tag{5}$$

3. Results and discussion

The following sections cover the characterization of the samples prior to the redox studies in the TGA, as well as the thermochemical redox yield. These results are used to explore the aspect of doping Sr as an A-site dopant on $Nd_{1-x}Sr_xMnO_3$.

Table 1. *Composition of synthesized samples as confirmed by EDS analysis*

S. No.	Sample ID	Sample Composition (as synthesized)	Sample composition (from EDS analysis)
1	NMXX	$NdMnO_3$	$Nd_{0.93}Mn_{1.07}O_3$
2	NSM82X	$Nd_{0.8}Sr_{0.2}MnO_3$	$Nd_{0.8}Sr_{0.2}Mn_{1.09}O_3$
3	NSM64X	$Nd_{0.6}Sr_{0.4}MnO_3$	$Nd_{0.57}Sr_{0.43}Mn_{1.05}O_3$
4	NSM46X	$Nd_{0.4}Sr_{0.6}MnO_3$	$Nd_{0.40}Sr_{0.6}Mn_{1.08}O_3$
5	NSM28X	$Nd_{0.2}Sr_{0.8}MnO_3$	$Nd0.18Sr_{0.82}Mn_{0.96}O_3$

Table 2. *Microstrain (ε) and average crystallite size (D, in nm) for each sample, determined using the Williamson-Hall (WH) plot from XRD data. The phase column indicates the phase purity and crystal structure. M: Multiphase, S: Single phase, O: Orthorhombic, Mono: Monoclinic, T: Tetragonal.*

S. No.	Sample ID	Micro-strain (ε)	Average crystallite size D (nm)	PDF-5+ Reference pattern	Phase
1	NMXX	0.0045	45.26	04-07-0114, 04-016-2207	M: O (44.9%) + Mono (55.1%)
2	NSM82X	0.0021	60.35	04-008-4443	S: O (100%)
3	NSM64X	0.0029	96.55	04-026-9068	S: O (100%)
4	NSM46X	0.0021	37.14	04-012-0580	S: T (100%)
5	NSM28X	0.0012	26.34	04-016-9100	S: T (100%)

3.1 Crystalline Structure & Morphology/Composition

Room-temperature powder XRD data in Figure 1(a) show the crystalline perovskite structure of Sr-doped $NdMnO_3$. *Figure 1*(b) indicates the peak shift in the X-ray diffractogram towards higher angles with increasing Sr doping in $Nd_{1-x}Sr_xMnO_3$. Takalkar et. Al., (2021) reported a similar peak shift in $La_{1-x}Sr_xMnO_3$ samples, where successive Sr doping caused the XRD peaks to shift towards higher angels [11]. However, various other literature i.e., Gao et al., (2023) observed a shift towards lower angles due to lattice expansion, as Sr^{+2} (with a larger ionic radii) substitutes Ce^{+3} (with a relatively smaller ionic radii) in $Ce_{1-x}Sr_xMnO_3$ [12]. Considering both explanations, since the Shannon's ionic Radii of Sr^{+2} is larger than that of La or Nd in a $La_{1-x}Sr_xMnO_3$/$Nd_{1-x}Sr_xMnO_3$ perovskites, the successive substitution of Sr^{+2} to replace Nd^{+3} can be attributed in terms of microstrain within the lattice rather than lattice expansion. Rietveld refinement indicates that $NdMnO_3$ is multiphasic with 44.9% Orthorhombic and 55.1 % monoclinic phase. Rest all samples are single phasic orthorhombic for 20 and 40% Sr doping. With successive Sr doping to 60 and 80%, the perovskite structure adopts a higher symmetry tetragonal structure instead of orthorhombic. Table 2 outlines the microstrain (ε) and the average crystallite size (D, in nm) determined using Wiliamson-Hall plot with XRD data for each sample (Figure 3). Among the doped samples, NSM64X (with 40% Sr doping) shows the highest microstrain and crystallite size. The increased microstrain within the lattice could potentially leverage a relatively facile Mn-O bond. Additionally, NSM64X has the highest average crystallite size, and may facilitate oxygen vacancies and charge movement within the lattice due to its relatively smaller grain boundaries compared to other samples.

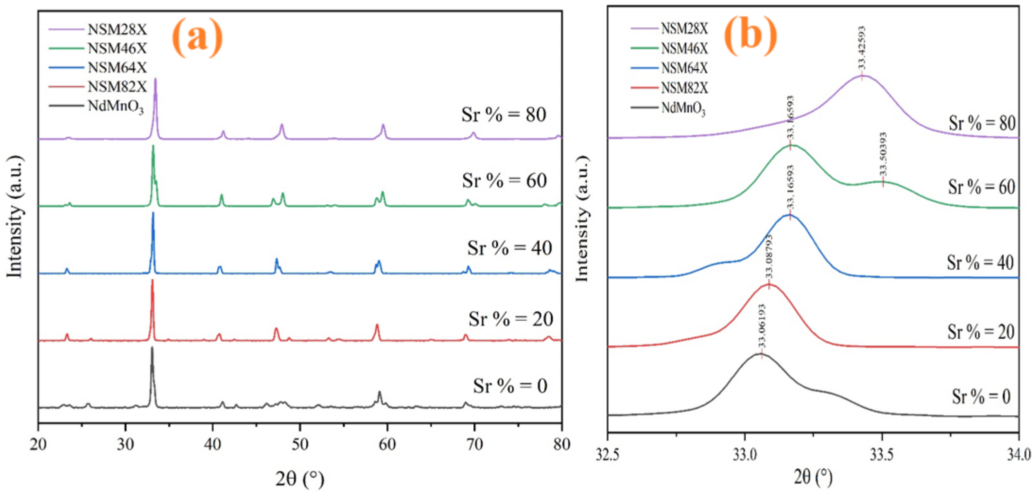

Figure 1. *(a) XRD diffractogram of* $Nd_{1-x}Sr_xMnO_3$ *samples. (b) Zoomed-in XRD pattern in the 2θ range of 32.5°-34.0° to visualize peak shift*

Figure 2(a-f) presents SEM images of $NdMnO_3$ and other doped samples. $NdMnO_3$ shows a smooth morphology with compactly structured large grains. However, yield data (Figure 4) show minimal redox activity for the undoped sample, consistent with findings from various literature sources on similar systems [11], [13], [14], [15], [16]. With successive Sr doping, the morphology becomes rough and porous, as shown in Figure 2(b-e). Figure 2(c) shows that the 40% Sr-doped sample ($Nd_{0.6}Sr_{0.4}MnO_3$) exhibits the highest degree of roughness and porosity compared to other samples. As evident from Figure 2(d-f), any Sr doping above 40% leads to material sintering, where grains start breaking down and the material starts agglomerating, resulting in reduced porosity. This ultimately leads to longer grain boundaries posing resistance to charge movement and lower yields. Hence, microstrain/average crystallite sizes shown in figure 3 closely correspond to the SEM images (figure 2). Figure 2(f) shows SEM image of an air-calcined perovskite particle. Table 1 enlists the EDS composition data of the air-calcined perovskite samples before redox testing, which fairly corresponds with the intended stoichiometry of the samples.

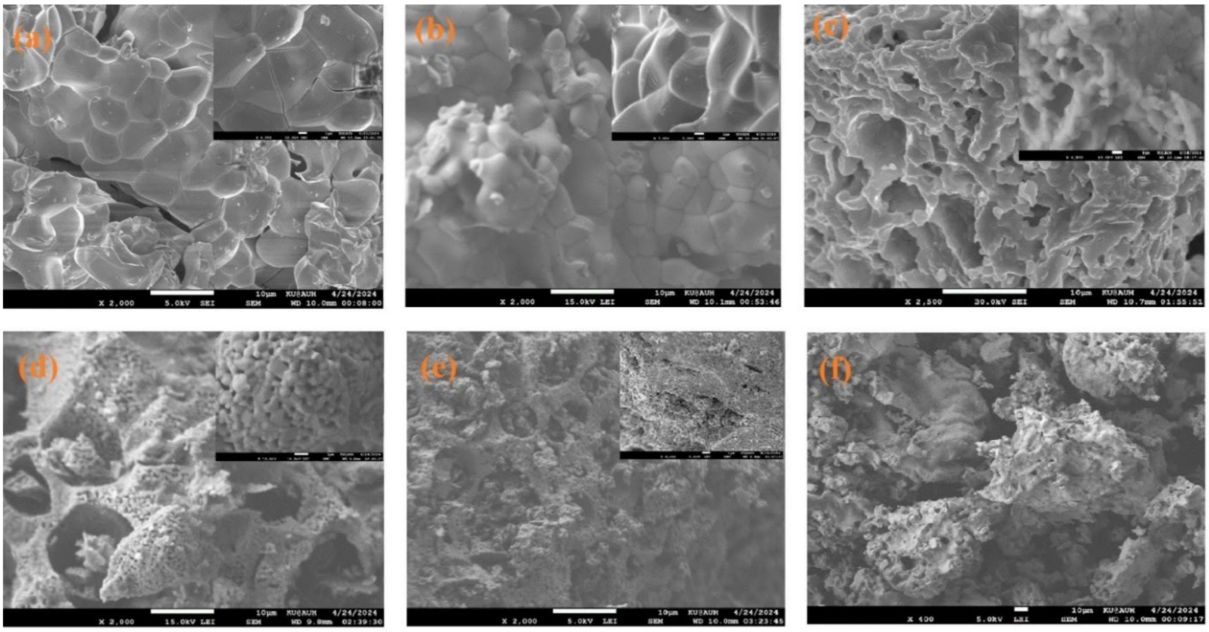

Figure 2. *SEM images of (a)* $NdMnO_3$ *(b) NSM82X (c) NSM64X (d) NSM46X (e) NSM28X (f) air-calcined perovskite particles*

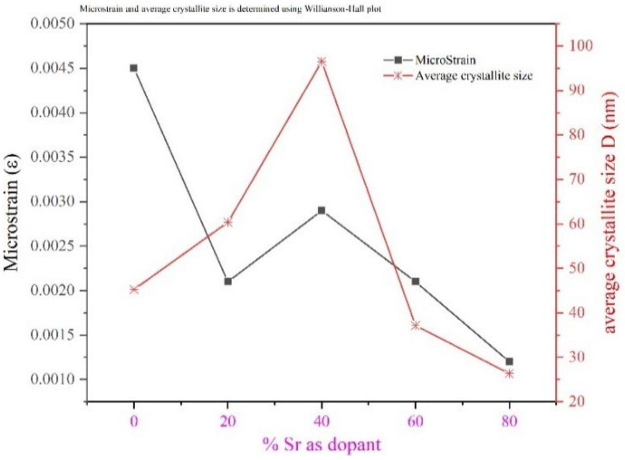

Figure 3. *Microstrain and average crystallite size of $Nd_{1-x}Sr_xMnO_3$ samples*

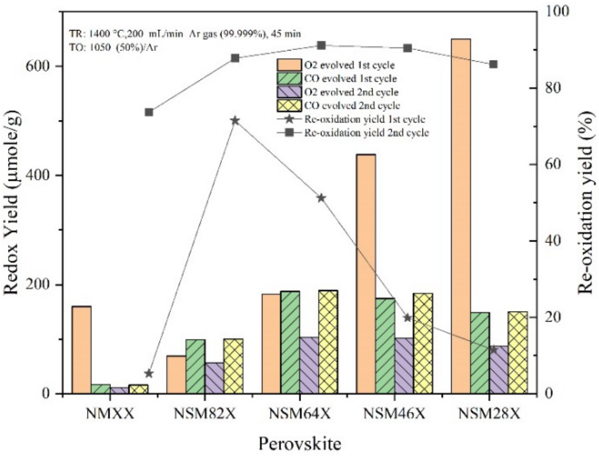

Figure 4. *Redox activity and re-oxidation yield of $Nd_{1-x}Sr_xMnO_3$ samples*

3.2 Thermochemical Redox Activity

Figure 4 shows the thermochemical redox yield and re-oxidation yield of the perovskite samples. The temporal thermogravimetric mass variation (%) with the temperature program for the 2-step thermochemical redox activity of $Nd_{1-x}Sr_xMnO_3$ is illustrated in Figure 5. This compliments the hypothesis that introducing Sr as an A-site dopant facilitates thermal reduction, i.e., more O_2 evolves with successive Sr substitution during the thermal reduction step, as supported by the literature [17]. During the first cycle of operation, the amount of O_2 evolved during thermal reduction increases with Sr doping, from 20% to 80% doping. The CO yield however is maximum for NSM64X. In the second cycle, the redox yield shows that 40% Sr doping produces the maximum O_2 yield (103.7 μmol-O_2/g) and CO yield (189.2 μmol-CO/g) during thermal reduction and oxidation steps, outperforming the other samples. These higher values of yield correlate with the crystalline structure and morphological characteristics discussed in Section 3.1.

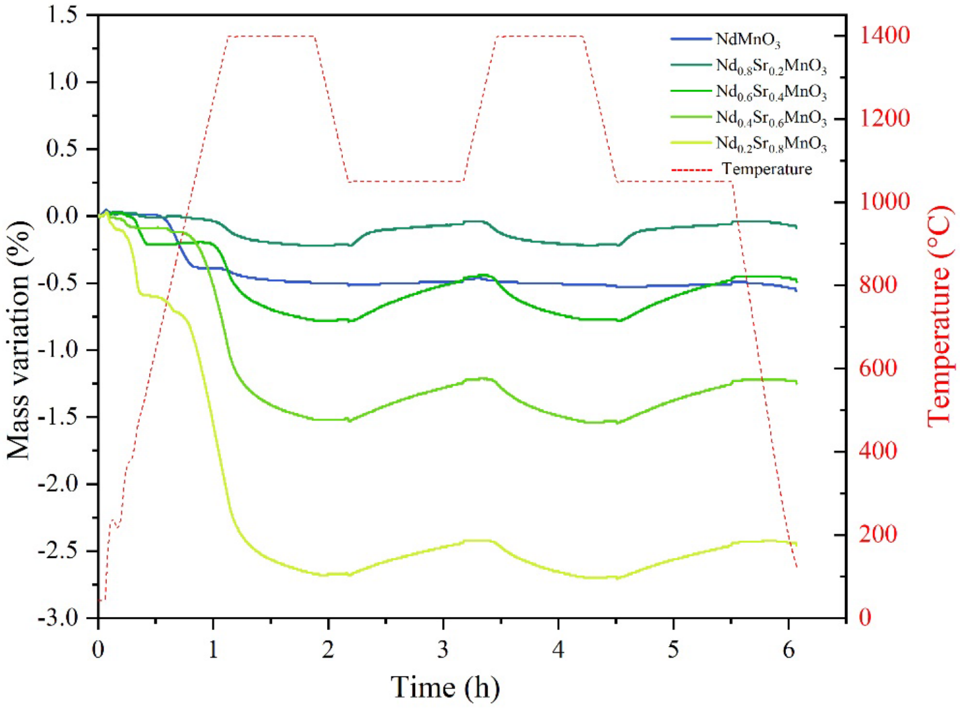

Figure 5. *Thermogravimetric data of* $Nd_{1-x}Sr_xMnO_3$ *samples*

Data from Figure 4 shows that NSM64X has the highest re-oxidation yield in the second cycle, at 91.2%. This indicates that 40 % Sr-doped $Nd_{1-x}Sr_xMnO_3$ has higher thermal stabilization such that the re-oxidation reaction has reached almost 91% of completion, demonstrating superior oxidation kinetics for NSM64X. The yield and re-oxidation data for the 60% Sr-doped sample (NSM46X) show close proximity to the NSM64X, though slightly lower in yield and re-oxidation values . The thermal reduction O_2 yield of NSM46X is 101.7 μmol-O_2/g, while its thermal re-oxidation CO yield is 184.0 μmol-CO/g, with a re-oxidation yield of 90.5% during the second cycle of operation.

TGA data from Figure 5 show that during the first cycle of operation, undoped $NdMnO_3$ undergoes mass variations in two distinct steps around 950 ℃. Typically, these changes could be attributed to the decomposition of the $SrCO_3$ phase, but since this sample is undoped, it can be inferred that $NdMnO_3$ decomposed into additional phases. In the second cycle, the re-oxidation yield of $NdMnO_3$ increases from 5.3% to 73.7%, which shows thermal stabilization of the material to some extent. However, the poor O_2 and CO yields suggest that $NdMnO_3$ is not suitable for potential application in 2-step thermochemical CO_2 splitting.

4. Conclusions

A series of neodymium-based perovskites were developed using the modified Pechini method, and their physico-chemical properties were characterized by XRD, EDS, and SEM. The activity of the perovskites was evaluated using thermogravimetric studies in a 2-step thermochemical process to calculate their redox and re-oxidation yields. The data revealed that the 40% Sr-doped sample (i.e., $Nd_{0.6}Sr_{0.4}MnO_3$) outperformed the other samples in terms of redox and reoxidation yields, with the 60% Sr-doped sample ($Nd_{0.4}Sr_{0.6}MnO_3$) being the next most promising candidate. Therefore, various compositions in the 40-60% Sr doping range should be tested experimentally to find the optimal Sr concentration. Additionally, the hypothesis of increased microstrain in $Nd_{0.6}Sr_{0.4}MnO_3$, based on the Williamson-Hall plot, should be further elucidated using XPS studies to assess any changes in the oxidation state of the tranisition metal cation (Mn^{3+}) for better understanding.

Author contributions

Conceptualization: K.A., Experimental work: M.U., S.A.; Writing original-draft preparation: M.U., K.A.; Writing-Editing & Review & supervision: K.A., G.P., G.K.; All authors discussed the results and contributed to the final manuscript.

Competing interests

The authors declare that they have no competing interests.

Funding

This project was financially supported by Khalifa University of Science and Technology under grant number RC2-2019-007, which is attributed to the Research and Innovation Center on CO_2 and Hydrogen (RICH).

Acknowledgement

The authors gratefully acknowledge the lab facilities at the RICH Center and Khalifa University Core Labs.

References

[1] L. Fu *et al.*, "Research progress on CO2 capture and utilization technology," Dec. 01, 2022, *Elsevier Ltd*. doi: 10.1016/j.jcou.2022.102260.
[2] C. F. Heuberger, I. Staffell, N. Shah, and N. Mac Dowell, "Quantifying the value of CCS for the future electricity system," *Energy Environ Sci*, vol. 9, no. 8, pp. 2497–2510, Aug. 2016, doi: 10.1039/c6ee01120a.
[3] X. Sun, S. Jiang, H. Huang, H. Li, B. Jia, and T. Ma, "Solar Energy Catalysis," Jul. 18, 2022, *John Wiley and Sons Inc*. doi: 10.1002/anie.202204880.
[4] U. Pelay, L. Luo, Y. Fan, D. Stitou, and M. Rood, "Thermal energy storage systems for concentrated solar power plants," 2017, *Elsevier Ltd*. doi: 10.1016/j.rser.2017.03.139.
[5] P. Denholm, J. C. King, C. F. Kutcher, and P. P. H. Wilson, "Decarbonizing the electric sector: Combining renewable and nuclear energy using thermal storage," *Energy Policy*, vol. 44, pp. 301–311, May 2012, doi: 10.1016/j.enpol.2012.01.055.
[6] G. Alva, Y. Lin, and G. Fang, "An overview of thermal energy storage systems," Feb. 01, 2018, *Elsevier Ltd*. doi: 10.1016/j.energy.2017.12.037.
[7] L. F. Cabeza, A. Solé, and C. Barreneche, "Review on sorption materials and technologies for heat pumps and thermal energy storage," *Renew Energy*, vol. 110, pp. 3–39, 2017, doi: 10.1016/j.renene.2016.09.059.
[8] A. H. Abedin and M. A. Rosen, "A Critical Review of Thermochemical Energy Storage Systems," 2011.
[9] T. O. L. Sunde, T. Grande, and M. A. Einarsrud, "Modified pechini synthesis of oxide powders and thin films," in *Handbook of Sol-Gel Science and Technology: Processing, Characterization and Applications*, Springer International Publishing, 2018, pp. 1089–1118. doi: 10.1007/978-3-319-32101-1_130.
[10] J. Jouannaux, A. Haeussler, M. Drobek, A. Ayral, S. Abanades, and A. Julbe, "Lanthanum manganite perovskite ceramic powders for CO2 splitting: Influence of Pechini synthesis parameters on sinterability and reactivity," *Ceram Int*, vol. 45, no. 12, pp. 15636–15648, Aug. 2019, doi: 10.1016/j.ceramint.2019.05.075.
[11] G. Takalkar *et al.*, "Thermochemical splitting of CO2 using solution combustion synthesized lanthanum–strontium–manganese perovskites," *Fuel*, vol. 285, Feb. 2021, doi: 10.1016/j.fuel.2020.119154.

[12] K. Gao *et al.*, “Remarkable solar thermochemical CO2 splitting performances based on Ce- and Al-doped SrMnO3 perovskites,” *Sustain Energy Fuels*, vol. 7, no. 4, pp. 1027–1040, Jan. 2023, doi: 10.1039/d2se01496c.

[13] Z. Chen *et al.*, “Sr- and Co-doped LaGaO3-δ with high O2 and H2 yields in solar thermochemical water splitting,” *J Mater Chem A Mater*, vol. 7, no. 11, pp. 6099–6112, 2019, doi: 10.1039/c8ta11957k.

[14] L. Wang *et al.*, “Experimental study on the high performance of Zr doped LaCoO3 for solar thermochemical CO production,” *Chemical Engineering Journal*, vol. 389, Jun. 2020, doi: 10.1016/j.cej.2020.124426.

[15] X. Liu *et al.*, “Ca- And Ga-Doped LaMnO3for Solar Thermochemical CO2Splitting with High Fuel Yield and Cycle Stability,” *ACS Appl Energy Mater*, vol. 4, no. 9, pp. 9000–9012, Sep. 2021, doi: 10.1021/acsaem.1c01274.

[16] G. Takalkar *et al.*, “Thermochemical splitting of CO2 using solution combustion synthesized LaMO3 (where, M = Co, Fe, Mn, Ni, Al, Cr, Sr),” *Appl Surf Sci*, vol. 509, Apr. 2020, doi: 10.1016/j.apsusc.2019.144908.

[17] B. Chen, H. Kildahl, H. Yang, Y. Ding, L. Tong, and L. Wang, “Thermochemical splitting of CO2 on perovskites for CO production – A review,” Mar. 01, 2024, *Elsevier B.V.* doi: 10.1016/j.jechem.2023.11.041.